

# Journal of Materials Chemistry A

Accepted Manuscript



This is an *Accepted Manuscript*, which has been through the Royal Society of Chemistry peer review process and has been accepted for publication.

*Accepted Manuscripts* are published online shortly after acceptance, before technical editing, formatting and proof reading. Using this free service, authors can make their results available to the community, in citable form, before we publish the edited article. We will replace this *Accepted Manuscript* with the edited and formatted *Advance Article* as soon as it is available.

You can find more information about *Accepted Manuscripts* in the [Information for Authors](#).

Please note that technical editing may introduce minor changes to the text and/or graphics, which may alter content. The journal's standard [Terms & Conditions](#) and the [Ethical guidelines](#) still apply. In no event shall the Royal Society of Chemistry be held responsible for any errors or omissions in this *Accepted Manuscript* or any consequences arising from the use of any information it contains.

## ARTICLE

# Facile preparation of three-dimensional Fe<sub>3</sub>O<sub>4</sub>/macroporous graphene composite for high-performance Li storage

Cite this: DOI: 10.1039/x0xx00000x

Received 00th January 2015,  
Accepted 00th January 2015

DOI: 10.1039/x0xx00000x

www.rsc.org/

Xiaoyu Lu<sup>a</sup>, Ronghua Wang<sup>a</sup>, Yang Bai<sup>a</sup>, Jingjing Chen<sup>a</sup> and Jing Sun<sup>a\*</sup>

Three-dimensional macroscopic Fe<sub>3</sub>O<sub>4</sub>/porous graphene (FPG) composite was prepared by a facile self-assemble method at room temperature using polystyrene spheres as template, followed by calcination treatment. The FPG with 3D macroporous graphene framework tightly anchored with Fe<sub>3</sub>O<sub>4</sub> nanoparticles (NPs) ensures reversible reaction and fast electron/Li<sup>+</sup> transport of the FPG electrode. Benefiting from the interconnected graphene framework and macropores, the FPG electrode shows decreasing SEI and contact resistances during long-term cyclic tests with lower contact resistance and faster Li<sup>+</sup> diffusion compared to the contrastive Fe<sub>3</sub>O<sub>4</sub>/GS composed of numerous 2D hybrid sheets. As anode material for LIBs, the FPG exhibits superb rate capabilities (1057, 843, 709, 569 and 500 mAh g<sup>-1</sup> at current densities of 200, 400, 800, 2000 and 4000 mA g<sup>-1</sup>) and excellent long-term cyclic performance of 859mAh g<sup>-1</sup> after 1000 cycles at 2 A g<sup>-1</sup> rate, which is much better than that of Fe<sub>3</sub>O<sub>4</sub>/GS.

## 1 Introduction

Rechargeable lithium-ion batteries (LIBs) have been widely used in portable devices and are gaining increasing attention in the field of hybrid electric vehicles and distributed power generation applications.<sup>1,2</sup> To realize higher energy density and power density, metal oxides (MO) of all kinds, possessing much higher capacity than commercially used graphite, as well as eco-friendliness and natural abundance, are explored and studied as promising anode materials of LIBs.<sup>3,4</sup> Among these transition metal oxides, Fe<sub>3</sub>O<sub>4</sub> is dominant for its high electric conductivity and high theoretical capacity of 922 mAh g<sup>-1</sup>.<sup>5</sup> However, Fe<sub>3</sub>O<sub>4</sub> based electrodes still suffer from poor cycling performance and rate capability owing to ineffective Li<sup>+</sup> and electron transport along with large specific volume changes upon cycling.<sup>6</sup> To address these issues, diverse strategies have been proposed through special nanostructure designing, amorphous carbon coating and constructing hybrid materials with carbon nanotube or graphene.<sup>7-11</sup>

Graphene, typically defined as monolayer of sp<sup>2</sup> carbon atoms packed into a honey comb crystal structure, has raised great research fever as electrode materials for LIBs owing to these features: First, large specific surface area and outstanding electrical conductivity are ideal for the storage and transport of Li<sup>+</sup> and electrons. Second, 2D graphene sheets with great mechanical properties can buffer volume changes during Li<sup>+</sup> insertion/extraction.<sup>12</sup> These advantages make graphene/MO composite a promising candidate for novel LIBs application. To date, the means to prepare Fe<sub>3</sub>O<sub>4</sub>/rGO hybrids are mainly divided into three categories: wrapping, encapsulating and anchoring.<sup>13-18</sup> Although enhanced specific capacity has been

obtained, some drawbacks of these hybrids as electrode material still exist. In the first two types, metal oxides still suffer from aggregation and pulverization due to their untight interaction with graphene sheets. The third type has problem with large interface contact resistance among numerous graphene-based nanosheets.<sup>19</sup> To deal with these problems, researchers have designed various materials with 3D porous electrical conductive framework, including carbon/graphene-based and metal-based composite for LIBs to facilitate effective electron and Li-ion transport in the electrode.<sup>20-29</sup> In a simplified mode of lithiation reactions in LIBs, electrons transport from current collector along conductive paths, while Li<sup>+</sup> diffuse through electrolyte and bulk material. They meet at the reactive sites and charge transfer process takes place. The electrochemical reactions are mostly determined by electron/Li<sup>+</sup> transport and solid-state reaction of Li<sup>+</sup> and MO. The electrode materials with 3D porous conductive framework possess (i) high electron conductivity in the continuous framework, (ii) large open pores filled with electrolyte for fast Li<sup>+</sup> diffusion and buffering volume changes, (iii) short Li-ion diffusion length in solid-state nanosized active material and (iv) large surface area with more reactive sites.<sup>25</sup> There are many ways to construct such 3D porous structure: e.g. self-assembly of graphene by hydrothermal method<sup>27, 28, 30</sup> and electrodeposition of conductive metal using spherical template.<sup>25</sup> Among these, 3D porous graphene framework prepared by sacrificial template is advantageous for tunable structure and apt to hybridize with MO.<sup>23, 24, 31</sup> However, complex synthesis processes of this method such as pH control, freeze drying and additional hydrothermal treatment to incorporate with MO limited its application.<sup>23, 32</sup> Moreover, the superior electrochemical performance of 3D macroporous graphene/MO compared to 2D

graphene/MO sheet-like composite and the mechanism behind have not yet been clearly understood.

Herein, we proposed a facile calcination synthesis of three-dimensional  $\text{Fe}_3\text{O}_4$  NPs/porous graphene (FPG) composite as anode materials for LIBs, using carboxylic polystyrene (c-PS) spheres as the template. Due to the strong electrostatic interaction between oppositely charged  $\text{Fe}(\text{OH})_3/\text{GO}$  sheets and c-PS spheres, self-assemble process of the two precursors was conducted at room temperature with no special treatment, followed by calcination treatment to remove the template. The as-prepared composite shows a continuous 3D macroporous graphene framework uniformly anchored with  $\sim 20$  nm  $\text{Fe}_3\text{O}_4$  NPs, exhibiting great morphological stability and electrochemical activity. Benefiting from the unique characteristics, the optimized FPG electrode displays enhanced rate capability (1057, 843, 709, 569 and 500  $\text{mAh g}^{-1}$  at 200, 400, 800, 2000 and 4000  $\text{mA g}^{-1}$ ) and cyclic stability at high current density (859  $\text{mAh g}^{-1}$  after 1000 cycles at 2  $\text{A g}^{-1}$ ), which is better than the  $\text{Fe}_3\text{O}_4/\text{GS}$  and most other  $\text{Fe}_3\text{O}_4/\text{graphene}$  hybrids reported.<sup>13, 33-36</sup> Further EIS analysis reveals that the superior performance of FPG can be explained by low contact resistance owing to interconnected graphene framework and faster ion diffusion owing to open macropores. The structure stability of FPG that brings about excellent long-term cyclic performance is confirmed by reduced internal resistances and SEM observations of FPG after cycling.

## 2 Experimental

### 2.1 Material preparation

**Preparation of c-PS spheres.** c-PS spheres were synthesized using a suspension polymerization method.<sup>37, 38</sup> In detail, 100 mL distilled water, 0.12 g  $\text{NaHCO}_3$ , 5 mL styrene and 0.5 mL acrylic acid were successively added into a three-necked reaction flask. After heated to 70 °C under magnetic stirring, 0.2 g potassium persulfate as initiator was added in the flask. The solution was kept at 70 °C for 6 h and then 90 °C for 1 h. After washed with distilled water and centrifuged for several times, c-PS was finally dispersed in water.

**Preparation of  $\text{Fe}(\text{OH})_3$  sol.** 0.27 g  $\text{FeCl}_3 \cdot 6\text{H}_2\text{O}$  was dissolved in 10 mL distilled water to get a  $\text{FeCl}_3$  solution. The solution was then dropped into 60 mL boiling distilled water and  $\text{Fe}(\text{OH})_3$  sol was obtained.

**Preparation of the FPG composite.** Graphene oxide (GO) was prepared using a modified Hummers' method and dispersed in deionized water.<sup>39, 40</sup> The  $\text{Fe}(\text{OH})_3$  sol was added into 80 mL GO solution (2  $\text{mg mL}^{-1}$ ) drop wise, followed by magnetic stirring for 30 min. Next, certain amount of c-PS solution (containing 70  $\text{mg c-PS}$ ) was dropped into the mixture while stirring. The resulting composite was collected after several washing and centrifugation and dried in vacuum oven at 80 °C. Finally, the product was transferred to a tube furnace and calcined at 550 °C for 2 h under Ar atmosphere. As a control,  $\text{Fe}_3\text{O}_4/\text{GS}$  was fabricated through the same process as FPG only without the addition of c-PS.

### 2.2 Material characterization

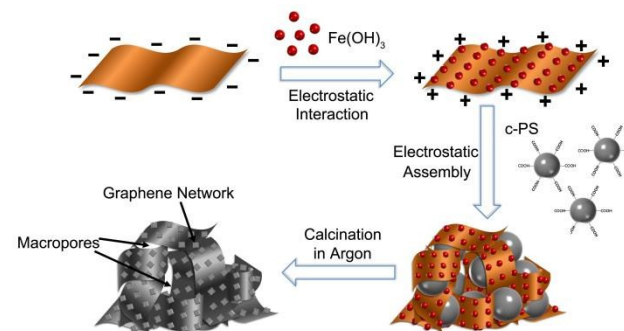
Thermogravimetry analysis was carried out with NETZSCH STA 449C in the temperature range 40-800 °C at a heating rate of 10 °C  $\text{min}^{-1}$  in air. Morphology of the samples was characterized with a field emission scanning microscope (Hitachi S4800) system and

transmission electron microscope (JEM-2100F at 200kV). Zeta potential was measured by Zetaplus in pure water at pH=5. X-ray diffraction (XRD) was carried out on D/max 2550V X-ray diffraction-meter with Cu-K $\alpha$  at  $\lambda=1.5406$ . Raman spectroscopy was recorded on a DXR Raman Microscope, Thermal Scientific Corporation, USA, with a 532 nm excitation length. The Fourier transform infrared (FT-IR) spectra were carried out on Thermo Scientific Nicolet iN10. X-ray photoelectron spectroscopy (XPS) analysis was conducted using twin anode gun, Mg K $\alpha$  (1253.6 eV) (Microlab 310F Scanning Auger Microprobe, VG SCIENTIFIC LTD).  $\text{N}_2$  adsorption/desorption isotherms were determined using a Micromeritics ASAP2010 Analyzer (USA).

### 2.3 Electrochemical measurements

Cyclic voltammetry (CV) test was taken on CHI660 electrochemical workstation in a voltage range of 3.0-0 V at a scan rate of 0.5  $\text{mV s}^{-1}$ . Nyquist plots were measured with the same workstation and all the half-cells were discharged to 0.005 V. Active materials were mixed with acetylene black and polyvinylidene fluoride (PVDF) binder in a weight ratio of 80:10:10 to form uniform slurry. After coating the slurry onto a copper foil, the electrode was dried in vacuum oven at 80 °C for 20 h. The electrolyte used was 1M  $\text{LiPF}_6$  in a 50:50 w/w mixture of ethylene carbonate (EC) and dimethyl carbonate (DMC). The half cells with lithium flake as counter electrode were assembled in CR2016 type coin cells in an argon-filled glove box with the concentration of moisture and oxygen below 1 ppm. Galvanostatical discharge and charge process were tested using a Land battery program-control test system (CT2001A) over a voltage range of 0.005-3.0 V versus  $\text{Li/Li}^+$ .

## 3 Results and discussion



**Scheme 1** Schematic illustration of the synthesis procedure for FPG.

The route for 3D macroscopic FPG material preparation is illustrated in Scheme 1. As we know, GO sheets in aqueous solution are usually negatively charged within a wide range of pH conditions for the abundant oxygen-containing groups on the surface and edges.<sup>17</sup> The exact pH range varied because of different degrees of oxidization. In our experiment, positively charged  $\text{Fe}(\text{OH})_3$  colloidal nanoparticles were firstly attracted onto negatively charged GO sheets (Zeta potential= $-28.84$  mV, Table S1) in a pH=5 aqueous solution, forming positively charged  $\text{Fe}(\text{OH})_3/\text{GO}$  nanosheets (Zeta potential= $27.77$  mV). The electrostatic repulsion between  $\text{Fe}(\text{OH})_3$  NPs and attraction between GO and  $\text{Fe}(\text{OH})_3$  ensured well dispersion and strong adhesion on GO surface of  $\text{Fe}(\text{OH})_3$  NPs. Moreover, such  $\text{Fe}(\text{OH})_3/\text{GO}$  hybrid sheets remained highly flexible, which can be manipulated to form 3D porous interconnected structure

with the help of *c*-PS template. Acrylic acid used in styrene polymerization decorated *c*-PS spheres with rich carboxylic groups, which endowed *c*-PS spheres with negatively charged surface (Zeta potential = -54.40 mV at pH=5) and aqueous solubility. When added into  $\text{Fe}(\text{OH})_3/\text{GO}$  suspension, *c*-PS spheres with average diameter of about 300 nm (Fig. S1) were entrapped in pliable  $\text{Fe}(\text{OH})_3/\text{GO}$  sheets, forming a  $\text{Fe}(\text{OH})_3/\text{GO}/c\text{-PS}$  mixture. Unlike the core-shell structure, the  $\text{Fe}(\text{OH})_3/\text{GO}$  sheets connected with each other forming a whole owing to their much larger 2D area than the diameter of *c*-PS.<sup>20</sup> It is noteworthy that all the above procedures were conducted at room temperature owing to strong electrostatic forces between oppositely charged  $\text{Fe}(\text{OH})_3/\text{GO}$  and  $\text{Fe}(\text{OH})_3/\text{GO}/c\text{-PS}$ . During the calcination treatment,  $\text{Fe}(\text{OH})_3$  and GO were converted to  $\text{Fe}_3\text{O}_4$  and rGO, respectively. Meanwhile, original *c*-PS spheres went through pyrolysis and carbonization processes.<sup>41, 42</sup> The released pyrolytic gaseous monomers helped creating open macropores in the FPG,<sup>43</sup> inducing the three-dimensional porous graphene framework anchored with nanosized  $\text{Fe}_3\text{O}_4$  particles.

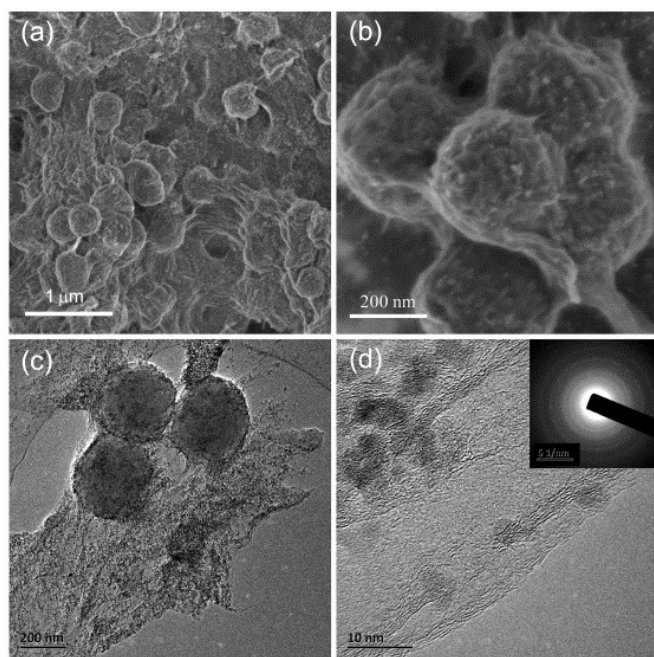


**Fig. 1** (a and b) SEM images of the  $\text{Fe}(\text{OH})_3/\text{GO}/c\text{-PS}$  at different magnification; (c) TEM image of the  $\text{Fe}(\text{OH})_3/\text{GO}/c\text{-PS}$ ; (d) HRTEM image of the  $\text{Fe}(\text{OH})_3/\text{GO}/c\text{-PS}$  at the fringe region, (inset of d) the corresponding SEAD pattern reveals polycrystalline  $\text{Fe}(\text{OH})_3$ .

As mentioned above, the unique structure of  $\text{Fe}(\text{OH})_3/\text{GO}/c\text{-PS}$  induced the formation of 3D macroporous FPG. SEM image (Fig. 1a) shows that *c*-PS spheres on the surface are covered with  $\text{Fe}(\text{OH})_3/\text{GO}$  sheets. Close packed *c*-PS spheres with  $\text{Fe}(\text{OH})_3/\text{GO}$  sheets on them are observed (Fig. 1b), for which we speculate that the majority of *c*-PS and  $\text{Fe}(\text{OH})_3/\text{GO}$  are arranged in a similar way. Further TEM observations are conducted after drastic ultrasonication and grind used to disperse the material. As shown in Fig. 1c, the *c*-PS spheres are still closely attached to  $\text{Fe}(\text{OH})_3/\text{GO}$  sheets, which suggests structural stability of  $\text{Fe}(\text{OH})_3/\text{GO}/c\text{-PS}$  prepared only by adding the three agents in proper order. The 3-5 nm polycrystalline  $\text{Fe}(\text{OH})_3$  particles show good dispersibility on

~5 layered GO sheets (Fig. 1d), which determines well-dispersed  $\text{Fe}_3\text{O}_4$  NPs that further inhibits agglomeration and pulverization of active material during  $\text{Li}^+$  insertion/extraction processes.

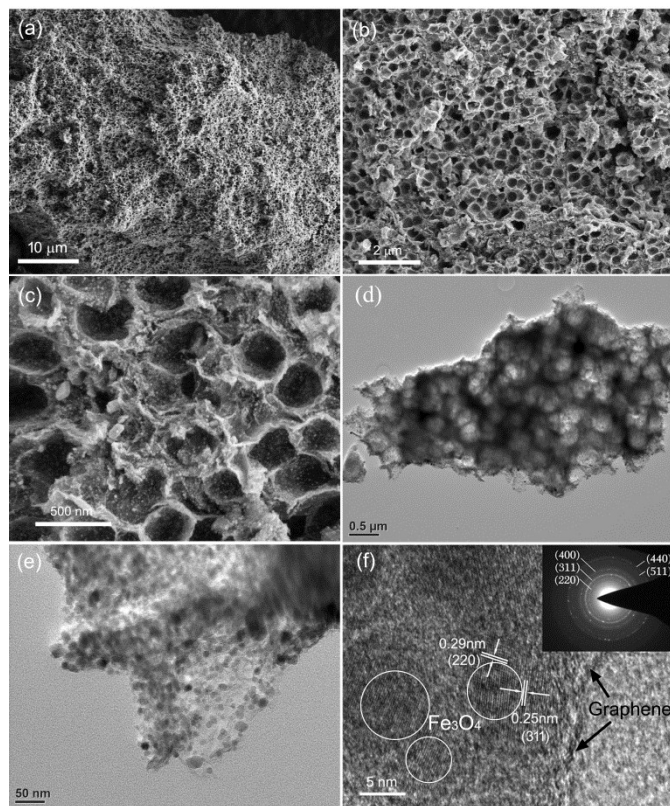


**Fig. 2** (a-c) SEM images of the FPG at different magnification; (d and e) TEM images of the FPG at different magnification; (f) HRTEM image of the FPG, the inset is the corresponding SAED pattern.

After the calcination treatment, the FPG with continuous  $\text{Fe}_3\text{O}_4/\text{GS}$  framework retains its original construction instead of collapsing after *c*-PS spheres vanish. SEM and TEM images (Fig. 2) of the as-prepared FPG composite exhibit a well-defined 3D hierarchical macroporous architecture. SEM images (Fig. 2a, b) show that the whole FPG composite surface is covered with numerous orderly arranged pores of about 300 nm in diameter. Closer observations (Fig. 2c) reveal a continuous thin-walled graphene framework with evenly dispersed  $\text{Fe}_3\text{O}_4$  NPs, which would facilitate efficient electron transport to active material. As shown in TEM image (Fig. 2d), the FPG owns a well-defined hierarchical structure with close-packed spherical macropores. Induced by the gaseous monomers released from the embedded *c*-PS spheres, these macropores are interconnected to each other and form a 3D open structure. On the graphene framework, 10-30 nm  $\text{Fe}_3\text{O}_4$  NPs are evenly dispersed (Fig. 2e), showing crystal growth from original  $\text{Fe}(\text{OH})_3$  (~5 nm). The interplanar spacing of  $\text{Fe}_3\text{O}_4$  NPs are 0.25 nm and 0.29 nm (Fig. 2f), corresponding to the (311) and (220) facet of magnetite  $\text{Fe}_3\text{O}_4$ , which is consistent with SAED pattern (inset of Fig. 2f). In comparison, the  $\text{Fe}_3\text{O}_4/\text{GS}$  composite with the same thermal treatment exhibits a completely different structure, in which numerous crumpled  $\text{Fe}_3\text{O}_4/\text{GS}$  sheets are randomly assembled (Fig. S2). When the

FPG composite is used as electrode for LIBs, the large porosity and intense adhesion of  $\text{Fe}_3\text{O}_4$  NPs on graphene framework would restrict expansion and contraction of  $\text{Fe}_3\text{O}_4$  NPs during cycling, which leads to enhanced cyclic performance. The small size of  $\text{Fe}_3\text{O}_4$  facilitates fast  $\text{Li}^+$  diffusion in bulk materials. Moreover, the 3D conductive graphene framework with interconnected open pores could shorten both electric and  $\text{Li}^+$  diffusion distances, which contributes to improved rate capability.

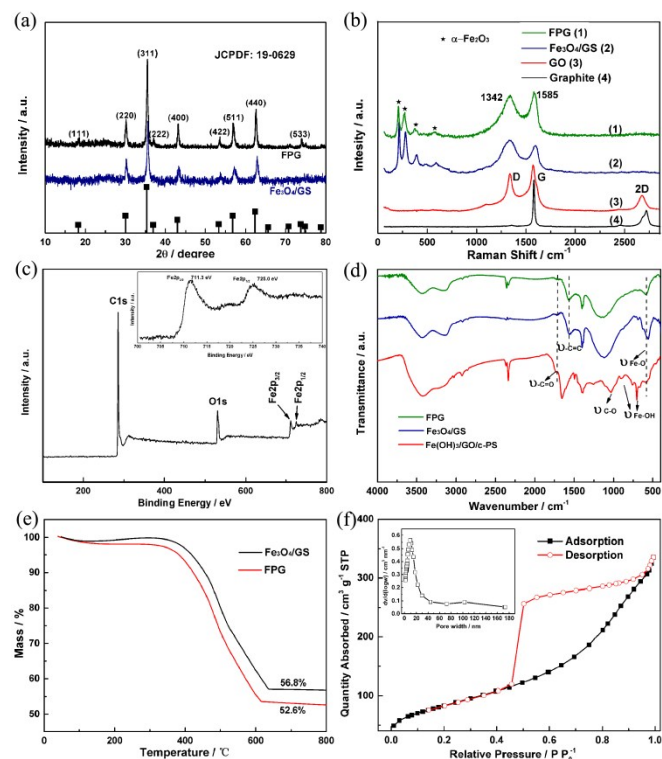


**Fig. 3** Sample characterization: (a) XRD patterns of FPG and  $\text{Fe}_3\text{O}_4/\text{GS}$ ; (b) TG curves of FPG and  $\text{Fe}_3\text{O}_4/\text{GS}$ ; (c) XPS spectrum of the FPG; (inset of c) Fe 2p core-level XPS spectrum; (d) FT-IR spectra of the FPG,  $\text{Fe}_3\text{O}_4/\text{GS}$  and  $\text{Fe}(\text{OH})_3/\text{GO}/\text{c-PS}$ ; (e) Raman spectra of FPG,  $\text{Fe}_3\text{O}_4/\text{GS}$ , GO and pristine graphite; (f) Nitrogen adsorption-desorption isotherms and (inset of f) pore size distribution of FPG.

XRD patterns of the FPG and  $\text{Fe}_3\text{O}_4/\text{GS}$  are shown in Fig. 3a, the peaks of both composites can well be indexed as magnetite  $\text{Fe}_3\text{O}_4$  (JCPDS No.19-0629), or cubic  $\gamma\text{-Fe}_2\text{O}_3$  (JCPDS No.39-1346). Average size of  $\text{Fe}_3\text{O}_4$  NPs in the FPG is calculated to be 24 nm by half peak width according to Scherrer Equation, which is consistent with the TEM observation. Raman spectra of the FPG and  $\text{Fe}_3\text{O}_4/\text{GS}$  (Fig. 3b) indicates the existence of  $\alpha\text{-Fe}_2\text{O}_3$  ( $A_{1g}$ : 212  $\text{nm}^{-1}$ ;  $E_g$ : 277, 377 and 573  $\text{nm}^{-1}$ ). This can be attributed to the decomposition of  $\text{Fe}_3\text{O}_4$  to  $\alpha\text{-Fe}_2\text{O}_3$  simulated by laser light (532 nm) used in Raman measurement.<sup>11, 44, 45</sup> The graphene hybrids show typical D band and G band at around 1344 and 1586  $\text{nm}^{-1}$ . The larger  $I_D/I_G$  ratio of FPG (0.92) than GO (0.81) indicates diminishing of  $\text{sp}^2$  hybridized carbon.<sup>46, 47</sup> Besides, the lower  $I_D/I_G$  ratio of FPG than  $\text{Fe}_3\text{O}_4/\text{GS}$  (1.20) is probably caused by the pyrolyzed residue of c-PS.<sup>48, 49</sup> To prove this, we further performed Raman spectra for calcined c-PS prepared with the same heat treatment for FPG (Fig. S3). The pyrolyzed residue of c-PS shows strong peaks and very low

$I_D/I_G$  ratio of 0.84 (Table S2) due to the numerous aromatic monomers in c-PS.<sup>7</sup> Fig. 3c shows wide scan XPS spectrum of FPG, which confirms the presence of C 1s, O 1s and Fe 2p. The core-level C 1s spectrum of FPG (Fig. S4) consists of three main components, accounting for C-C/C=C (285.0 eV), C-O (286.5 eV), C=O (287.6 eV). FPG is well reduced according to the large C/O ratio.<sup>28</sup> The peaks located at 711.3 eV and 725.0 eV is attributed to Fe 2p<sub>3/2</sub> and Fe 2p<sub>1/2</sub>, respectively, and there are no obvious satellites for  $\gamma\text{-Fe}_2\text{O}_3$ .<sup>50-52</sup> Fourier transform infrared (FT-IR) spectra of FPG,  $\text{Fe}_3\text{O}_4/\text{GS}$  and  $\text{Fe}(\text{OH})_3/\text{GO}/\text{c-PS}$  are shown in Fig. 3d. Instead of typical multi-peaks of  $\gamma\text{-Fe}_2\text{O}_3$ , only one peak of FPG at 585  $\text{cm}^{-1}$  is found and assigned to Fe-O stretching vibration modes in stoichiometric  $\text{Fe}_3\text{O}_4$ .<sup>28, 33, 36, 50</sup> The peaks of  $\text{Fe}(\text{OH})_3/\text{GO}/\text{c-PS}$  at 702, 755 and 898  $\text{cm}^{-1}$  are possibly attributed to bending vibrations of Fe-OH.<sup>28</sup> Those ones disappear in the spectrum of FPG due to the transformation from  $\text{Fe}(\text{OH})_3$  to  $\text{Fe}_3\text{O}_4$ . The absorption bands of carboxyl C=O at 1720  $\text{cm}^{-1}$  and epoxy C-O at 1030  $\text{cm}^{-1}$  are obviously decreased after calcination, showing effective reduction of graphene in FPG.<sup>33, 53</sup> Thermogravimetry analysis (TGA) was conducted to determine the  $\text{Fe}_3\text{O}_4$  content in FPG and  $\text{Fe}_3\text{O}_4/\text{GS}$ . Weight loss before 200 °C is attributed to water gasification. After heating to 800 °C, the FPG is completely converted to  $\text{Fe}_2\text{O}_3$ , with an overall weight loss of 47.4 wt%. According to this,  $\text{Fe}_3\text{O}_4$  contents in the FPG and  $\text{Fe}_3\text{O}_4/\text{GS}$  hybrids are calculated to be 51.8 wt% and 55.3 wt%, respectively (Fig. 3e). The nitrogen adsorption-desorption isotherms of the FPG shown in Fig. 3f is Type IV, with a H2 hysteresis loop at a relative pressure of 0.5-1 ( $P/P_0$ ). The BET

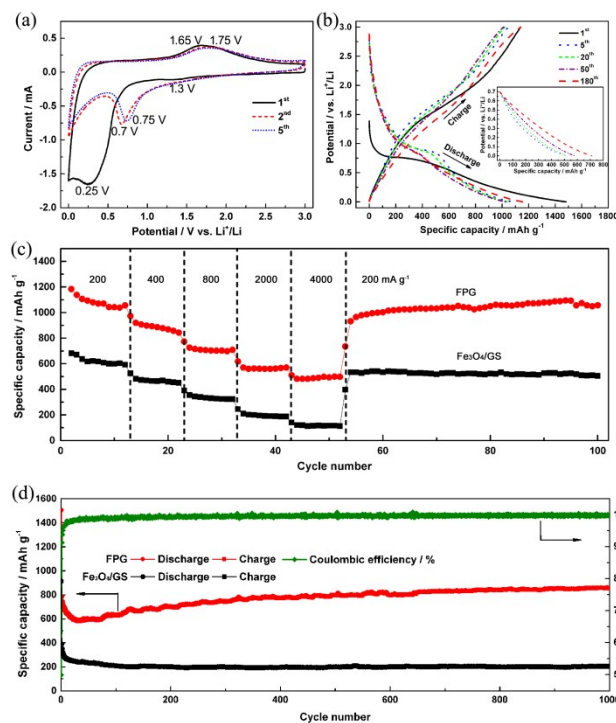


**Fig. 4** (a) Cyclic voltammograms for the 1<sup>st</sup>, 2<sup>nd</sup> and 5<sup>th</sup> cycles of FPG electrode; (b) Charge-discharge voltage profiles of FPG electrode at current density of 100  $\text{mA g}^{-1}$ , the inset is discharge voltage profiles of FPG between 0.7 V and 0.005 V; (c) Rate capabilities of FPG and  $\text{Fe}_3\text{O}_4/\text{GS}$  electrodes at different current densities; (d) Long-term cyclic performance of FPG and  $\text{Fe}_3\text{O}_4/\text{GS}$  electrodes at current density of 2  $\text{A g}^{-1}$ .

surface area of this FPG is  $301.7 \text{ m}^2 \text{ g}^{-1}$ , while  $\text{Fe}_3\text{O}_4/\text{GS}$  shows a slightly larger value of  $371.9 \text{ m}^2 \text{ g}^{-1}$  (Fig. S5). On one hand, the typical  $\sim 300 \text{ nm}$  macropores in FPG contribute little to the total BET surface.<sup>54</sup> (inset of Fig. 3f) On the other hand, the c-PS residue could reduce the BET by taking up some weight proportion. In a word, the FPG is similar to  $\text{Fe}_3\text{O}_4/\text{GS}$  in most characterization except for the unique 3D hierarchical porous structure by rationally design.

All the electrochemical tests of the FPG and  $\text{Fe}_3\text{O}_4/\text{GS}$  are carried out in a coin cell. To evaluate the cyclic performance of the FPG, we performed cyclic voltammetry test at  $0.5 \text{ mV s}^{-1}$  scan rate in 0-3.0 V voltage range. As shown in Fig. 4a, the FPG exhibits a shoulder peak at about 1.3 V in the first cycle, corresponding to diffusion of  $\text{Li}^+$  into  $\text{Fe}_3\text{O}_4$  crystal lattice forming  $\text{Li}_x\text{Fe}_3\text{O}_4$ ,<sup>8, 55</sup> but it disappears in the following cycles. A broad peak at  $\sim 0.25 \text{ V}$  reveals reduction reaction from  $\text{Fe}^{3+}$  and  $\text{Fe}^{2+}$  to  $\text{Fe}^0$ , as well as Li-ion insertion into graphene layers and surface. Then the only reduction peak shifts to a higher voltage with lower current response and narrower peak. On the other hand, broad oxidation peaks at  $\sim 1.65 \text{ V}$ , which could be attributed to the oxidation reaction from  $\text{Fe}^0$  to  $\text{Fe}^{2+}$  and  $\text{Fe}^{3+}$ , are found in the 1<sup>st</sup> and subsequent anodic processes. It is noteworthy that from the 2<sup>nd</sup> sweep cycle, the CV peaks of different cycles move to  $\sim 1.75 \text{ V}$  and overlap on one another, which indicates good reversibility of the discharge-charge reaction of the composite.

Long-term cyclic performance and rate capability of the FPG and  $\text{Fe}_3\text{O}_4/\text{GS}$  electrodes are performed with galvanostatic discharge-charge measurements at various current densities from 100 to  $4000 \text{ mA g}^{-1}$ . The discharge and charge curves of FPG shown in Fig. 4b reveal a reversible capacity of  $1154 \text{ mAh g}^{-1}$  at  $100 \text{ mA g}^{-1}$  after 180 cycles. The 1<sup>st</sup> discharge and charge capacities are  $1480.9$  and  $1139.1 \text{ mAh g}^{-1}$ . The low coulombic efficiency of  $76.9 \%$  is mainly due to the solid electrolyte interface (SEI) formation and other irreversible electrochemical reactions.<sup>9</sup> It rises rapidly to  $93.9 \%$  in the 2<sup>nd</sup> cycle and retains above  $98.5 \%$  after 25 cycles (Fig. S6). The specific capacity of FPG slightly decreases in the first 50 cycles, then increases gradually in the following cycles. Taking the CV results into consideration, conversion reaction of ferric oxide mostly takes place above  $0.7 \text{ V}$ . As a result, we separate the overall discharge capacity into two parts: the capacity owing to  $\text{Fe}_3\text{O}_4$  conversion reaction and other  $\text{Li}^+$  storage mostly contributed by graphene framework (inset of Fig. 4b).<sup>49</sup> The first part of capacity declines from  $563.2 \text{ mAh g}^{-1}$  (5<sup>th</sup>),  $523.4 \text{ mAh g}^{-1}$  (20<sup>th</sup>) to  $441.5 \text{ mAh g}^{-1}$  (50<sup>th</sup>) and thereafter keeps stable until the 180<sup>th</sup> cycle ( $442.1 \text{ mAh g}^{-1}$ ), which implies that the  $\text{Fe}_3\text{O}_4$  NPs undergoes limited pulverization and agglomeration in the first few cycles. Invertible reactions are acquired afterwards thanks to nanosized  $\text{Fe}_3\text{O}_4$  and confinement effect of graphene in FPG. The capacities between 0.7-0.005 V display an increasing tendency from  $518.5 \text{ mAh g}^{-1}$  (5<sup>th</sup>),  $523.2$  (20<sup>th</sup>),  $582.6 \text{ mAh g}^{-1}$  (50<sup>th</sup>) to  $712.4 \text{ mAh g}^{-1}$  (180<sup>th</sup>). Such enhancement is attributed to the large specific surface area for surface storage and structural stability of FPG, which endow stable SEI formation. As a result, capacity loss occurs in the first few cycles, while enhanced surface  $\text{Li}^+$  storage take the dominant position in the subsequent cycles. Compared to the  $\text{Fe}_3\text{O}_4/\text{GS}$  electrode (Fig. 4c), FPG shows better performance at different galvanostatic conditions. At current density of  $200 \text{ mA g}^{-1}$ , the FPG and  $\text{Fe}_3\text{O}_4/\text{GS}$  electrodes exhibit capacities of  $1057$  and  $603.3 \text{ mAh g}^{-1}$ , respectively. When current densities are changed to 400,

800, 2000, 4000 and  $200 \text{ mA g}^{-1}$ , the FPG shows capacity retention of  $79.8 \%$ ,  $67.1 \%$ ,  $53.9 \%$ ,  $47.2 \%$  and  $100 \%$ . However, the  $\text{Fe}_3\text{O}_4/\text{GS}$  electrode has only  $75.5 \%$ ,  $53.7 \%$ ,  $31.1 \%$ ,  $18.8 \%$  and  $84.4 \%$  of capacity retention. In a long-term cyclic performance test at current density as high as  $2 \text{ A g}^{-1}$ , the FPG electrode shows a reversible discharge capacity of  $859 \text{ mAh g}^{-1}$  even after 1000 cycles, compared to only  $201 \text{ mAh g}^{-1}$  for  $\text{Fe}_3\text{O}_4/\text{GS}$ . To better evaluate the performance of FPG, the important and recent works on  $\text{Fe}_3\text{O}_4/\text{graphene}$  electrode are listed on Table S3 for comparison. The specific capacity of FPG at low rate ( $0.1 \text{ A g}^{-1}$ ) is comparable to other works. We suppose that the relatively low  $\text{Fe}_3\text{O}_4$  weight ratio ( $52.6 \text{ wt}\%$ ) in FPG makes it not so outstanding at low rate. However, the performance of FPG at high rates is specially superior to  $\text{Fe}_3\text{O}_4/\text{graphene}$  with 2D sheet-like construction at present (references are listed in the Supplementary Information). The advantages owing to 3D interconnected graphene framework of FPG are evident, especially at high current densities. In the control  $\text{Fe}_3\text{O}_4/\text{GS}$  electrode, numerous sheets are randomly assembled, causing much longer diffusion paths for electron/ $\text{Li}^+$  and severe polarization effect during fast charge/discharge process.<sup>19</sup> In addition, the FPG with large porosity is more capable of buffering volume changes during cycling, which greatly enhances the cycleability.

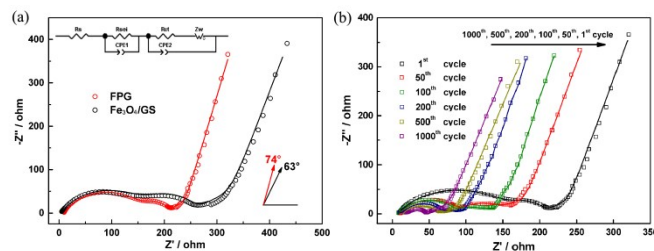


**Fig. 5** Nyquist plots of (a) FPG and  $\text{Fe}_3\text{O}_4/\text{GS}$  electrodes after first discharge and (b) FPG electrode after various number of cycles at current density of  $2 \text{ A g}^{-1}$ . Solid lines in both figures are fitted results using equivalent circuit model in Fig. 5a inset.

To verify the excellent performance of the FPG electrodes, we performed electrochemical impedance spectroscopy (EIS) in comparison with  $\text{Fe}_3\text{O}_4/\text{GS}$ . The Nyquist plots of both two samples are shown in Fig. 5a with a frequency range of 100 kHz to 0.001 Hz. The solid electrolyte interface resistance ( $R_{\text{SEI}}$ ) and the charge transfer resistance ( $R_{\text{ct}}$ ) are simulated with an equivalent circuit model (Fig. 5a inset) and the results are displayed in Fig. S7. Similar plots at high frequency suggest comparable  $R_{\text{SEI}}$  conditions for both samples. Compared to  $\text{Fe}_3\text{O}_4/\text{GS}$ , the diameters of the semi-circles for the FPG electrode at medium frequency is much smaller, which indicates decreased contact and charge transfer resistance.<sup>30, 56</sup> In the low frequency region, the FPG electrode exhibits a shortened and more inclined line with a slope of  $72^\circ$  ( $63^\circ$  for  $\text{Fe}_3\text{O}_4/\text{GS}$ ), indicating faster  $\text{Li}^+$  diffusion in the FPG.<sup>57</sup> In addition, the Nyquist plots of FPG show a trend of depressed semicircles at high/medium frequency and shortened tail at low frequency during cycling (Fig. 5b).  $R_{\text{SEI}}$  and  $R_{\text{ct}}$  are  $154 \Omega$  and  $39 \Omega$  at the first cycle, decreasing gradually to  $25 \Omega$  and  $2 \Omega$  at the 1000<sup>th</sup> cycle, respectively. These results suggest that the FPG with 3D structure retains well in morphology during high rate cycles. Moreover, stabilized and partially reversible SEI film forms after a few cycles, which contributes to the enhancement of specific capacity during long-term cycling.<sup>58-60</sup>

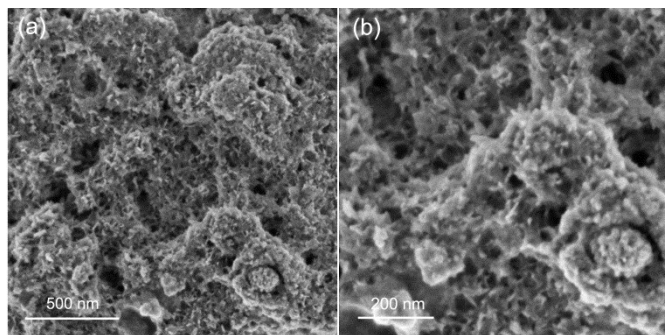


**Fig. 6** SEM images of the FPG after 1000 cycles at  $2 \text{ A g}^{-1}$  current density and charged to 3.0 V.

SEM images of the FPG electrode after 1000 cycles at  $2 \text{ A g}^{-1}$  are shown in Fig. 6. The 3D porous structure remains well in shape, with some surface maybe covered with aggregated ferric oxides or SEI film. Although the original macropores are no longer found, numerous smaller pores appear instead, which are caused by extension and contraction effect as we suppose. The excellent structural stability of the interconnected 3D macroporous FPG guarantees stable SEI film formation and fast electron/Li-ion transformation even at high rate for long-term cycling.

#### 4 Conclusion

In summary, we have developed a facile calcination method to rationally design 3D  $\text{Fe}_3\text{O}_4$ /porous graphene composite as high performance anode materials for LIBs. Well crystallized  $\text{Fe}_3\text{O}_4$  NPs of  $\sim 20 \text{ nm}$  in size are homogeneously anchored on 3D graphene framework with  $\sim 300 \text{ nm}$  open macropores. This macroporous structure is established through strong interaction between oppositely charged  $\text{Fe}(\text{OH})_3/\text{GO}$  sheets and c-PS spheres in moderate conditions. In applications of lithium-ion battery electrode, the porous feature of FPG can help buffering volume changes of  $\text{Fe}_3\text{O}_4$  and greatly enhancing electrolyte/material interfacial reactivity. As a result, such 3D macroporous FPG shows superior rate capacity and long-term cyclic performance compared to the  $\text{Fe}_3\text{O}_4/\text{GS}$ . The good structural integrity of FPG after long-term cycles at high rate proves its ability to buffer volume changes and endow fast electron/ion transport. Lower electrode contact resistance of FPG than  $\text{Fe}_3\text{O}_4/\text{GS}$  with faster  $\text{Li}^+$  diffusion is further confirmed by EIS analysis, which theoretically explains why FPG has much better performance. Our work emphasizes the advantages in rationally designing metal oxide/carbon composite with porous sculpture. The simplicity of this method makes it promising in combining precise control of hierarchical morphology from macro to micro and mass production.

#### Acknowledgements

This work is supported by the 973 Project (2012CB932303), the National Natural Science Foundation of China (Grant No. 50972153, 51072215 and 51172261).

#### Notes and references

<sup>a</sup> The State Key Lab of High Performance Ceramics and Superfine Microstructure, Shanghai Institute of Ceramics, Chinese Academy of Sciences, 1295 Ding Xi Road, Shanghai 200050, China

<sup>†</sup> Electronic Supplementary Information (ESI) available. See DOI: 10.1039/b000000x/

1. J. B. Goodenough and Y. Kim, *Chemistry of Materials*, 2010, **22**, 587-603.
2. A. S. Arico, P. Bruce, B. Scrosati, J. M. Tarascon and W. van Schalkwijk, *Nat Mater*, 2005, **4**, 366-377.
3. M. V. Reddy, G. V. Subba Rao and B. V. Chowdari, *Chemical reviews*, 2013, **113**, 5364-5457.
4. P. Poizot, S. Laruelle, S. Grugeon, L. Dupont and J. M. Tarascon, *Nature*, 2000, **407**, 496-499.
5. Y. H. Chang, J. Li, B. Wang, H. Luo, H. Y. He, Q. Song and L. J. Zhi, *Journal of Materials Chemistry A*, 2013, **1**, 14658-14665.
6. L. Zhang, H. B. Wu and X. W. D. Lou, *Advanced Energy Materials*, 2014, **4**, 1300958.
7. Y. Su, S. Li, D. Wu, F. Zhang, H. Liang, P. Gao, C. Cheng and X. Feng, *ACS nano*, 2012, **6**, 8349-8356.
8. P. Lian, X. Zhu, H. Xiang, Z. Li, W. Yang and H. Wang, *Electrochimica Acta*, 2010, **56**, 834-840.
9. S. M. Yuan, J. X. Li, L. T. Yang, L. W. Su, L. Liu and Z. Zhou, *ACS applied materials & interfaces*, 2011, **3**, 705-709.
10. W.-M. Zhang, X.-L. Wu, J.-S. Hu, Y.-G. Guo and L.-J. Wan, *Advanced Functional Materials*, 2008, **18**, 3941-3946.
11. J. Z. Liu, J. F. Ni, Y. Zhao, H. B. Wang and L. J. Gao, *Journal of Materials Chemistry A*, 2013, **1**, 12879-12884.
12. S. Han, D. Wu, S. Li, F. Zhang and X. Feng, *Small*, 2013, **9**, 1173-1187.
13. Z.-S. Wu, G. Zhou, L.-C. Yin, W. Ren, F. Li and H.-M. Cheng, *Nano Energy*, 2012, **1**, 107-131.
14. J. Su, M. Cao, L. Ren and C. Hu, *The Journal of Physical Chemistry C*, 2011, **115**, 14469-14477.
15. R. H. Wang, C. H. Xu, J. Sun, L. Gao and C. C. Lin, *Journal of Materials Chemistry A*, 2013, **1**, 1794-1800.
16. D. Chen, G. Ji, Y. Ma, J. Y. Lee and J. Lu, *ACS applied materials & interfaces*, 2011, **3**, 3078-3083.
17. M. Du, C. Xu, J. Sun and L. Gao, *Journal of Materials Chemistry A*, 2013, **1**, 7154-7158.
18. S. K. Behera, *Chemical communications*, 2011, **47**, 10371-10373.
19. Y. Gong, S. Yang, Z. Liu, L. Ma, R. Vajtai and P. M. Ajayan, *Advanced materials*, 2013, **25**, 3979-3984.
20. P. Wu, H. Wang, Y. Tang, Y. Zhou and T. Lu, *ACS applied materials & interfaces*, 2014, **6**, 3546-3552.
21. Q. Zhu, P. Wu, J. Zhang, W. Zhang, Y. Zhou, Y. Tang and T. Lu, *ChemSusChem*, 2015, **8**, 131-137.
22. J. Li, P. Wu, Y. Tang, X. Xu, Y. Zhou, Y. Chen and T. Lu, *CrystEngComm*, 2013, **15**, 10340-10345.
23. X. Liu, J. Cheng, W. Li, X. Zhong, Z. Yang, L. Gu and Y. Yu, *Nanoscale*, 2014, **6**, 7817-7822.
24. B. G. Choi, M. Yang, W. H. Hong, J. W. Choi and Y. S. Huh, *ACS nano*, 2012, **6**, 4020-4028.
25. H. Zhang, X. Yu and P. V. Braun, *Nature nanotechnology*, 2011, **6**, 277-281.
26. S. Nardecchia, D. Carriazo, M. L. Ferrer, M. C. Gutierrez and F. del Monte, *Chemical Society reviews*, 2013, **42**, 794-830.
27. Y. Gong, S. Yang, L. Zhan, L. Ma, R. Vajtai and P. M. Ajayan, *Advanced Functional Materials*, 2014, **24**, 125-130.
28. H. P. Cong, X. C. Ren, P. Wang and S. H. Yu, *ACS nano*, 2012, **6**, 2693-2703.
29. H. Yin, S. Zhao, J. Wan, H. Tang, L. Chang, L. He, H. Zhao, Y. Gao and Z. Tang, *Advanced materials*, 2013, **25**, 6270-6276.
30. W. Wei, S. Yang, H. Zhou, I. Lieberwirth, X. Feng and K. Mullen, *Advanced materials*, 2013, **25**, 2909-2914.
31. D. Fan, Y. Liu, J. He, Y. Zhou and Y. Yang, *Journal of Materials Chemistry*, 2012, **22**, 1396-1402.

32. D. Ma, S. Yuan and Z. Cao, *Chinese Science Bulletin*, 2014, **59**, 2017-2023.
33. B. Li, H. Cao, J. Shao and M. Qu, *Chemical communications*, 2011, **47**, 10374-10376.
34. G. Zhou, D.-W. Wang, F. Li, L. Zhang, N. Li, Z.-S. Wu, L. Wen, G. Q. Lu and H.-M. Cheng, *Chemistry of Materials*, 2010, **22**, 5306-5313.
35. L. Ji, Z. Tan, T. R. Kuykendall, S. Aloni, S. Xun, E. Lin, V. Battaglia and Y. Zhang, *Physical chemistry chemical physics : PCCP*, 2011, **13**, 7170-7177.
36. G. Wang, T. Liu, X. Xie, Z. Ren, J. Bai and H. Wang, *Materials Chemistry and Physics*, 2011, **128**, 336-340.
37. X. Huang, H. Yu, J. Chen, Z. Lu, R. Yazami and H. H. Hng, *Advanced materials*, 2014, **26**, 1296-1303.
38. Z. Y. Lu, Y. Q. Qin, J. Y. Fang, J. Sun, J. Li, F. Q. Liu and A. S. Yang, *Nanotechnology*, 2008, **19**, 055602.
39. W. S. Hummers and R. E. Offeman, *Journal of the American Chemical Society*, 1958, **80**, 1339-1339.
40. C. H. Xu, J. Sun and L. Gao, *Journal of Materials Chemistry*, 2012, **22**, 975-979.
41. R. W. J. Westerhout, J. Waanders, J. A. M. Kuipers and W. P. M. van Swaaij, *Industrial & Engineering Chemistry Research*, 1997, **36**, 1955-1964.
42. W. W. Lukens and G. D. Stucky, *Chemistry of Materials*, 2002, **14**, 1665-1670.
43. H. Wang, D. Zhang, T. Yan, X. Wen, J. Zhang, L. Shi and Q. Zhong, *Journal of Materials Chemistry A*, 2013, **1**, 11778.
44. M. Sathish, T. Tomai and I. Honma, *Journal of Power Sources*, 2012, **217**, 85-91.
45. I. Chourpa, L. Douziech-Eyrolles, L. Ngaboni-Okassa, J. F. Fouquenot, S. Cohen-Jonathan, M. Souce, H. Marchais and P. Dubois, *The Analyst*, 2005, **130**, 1395-1403.
46. A. C. Ferrari, J. C. Meyer, V. Scardaci, C. Casiraghi, M. Lazzeri, F. Mauri, S. Piscanec, D. Jiang, K. S. Novoselov, S. Roth and A. K. Geim, *Physical Review Letters*, 2006, **97**, 187401.
47. L. M. Malard, M. A. Pimenta, G. Dresselhaus and M. S. Dresselhaus, *Physics Reports*, 2009, **473**, 51-87.
48. W. Gao, Y. Wan, Y. Dou and D. Zhao, *Advanced Energy Materials*, 2011, **1**, 115-123.
49. J. Zhu, D. Yang, X. Rui, D. Sim, H. Yu, H. H. Hng, H. E. Hoster, P. M. Ajayan and Q. Yan, *Small*, 2013, **9**, 3390-3397.
50. P. Wu, N. Du, H. Zhang, J. Yu and D. Yang, *The Journal of Physical Chemistry C*, 2011, **115**, 3612-3620.
51. L. Fan, B. Li, D. W. Rooney, N. Zhang and K. Sun, *Chemical communications*, 2015, **51**, 1597-1600.
52. S. H. Choi and Y. C. Kang, *Carbon*, 2014, **79**, 58-66.
53. M. Zong, Y. Huang, Y. Zhao, X. Sun, C. Qu, D. Luo and J. Zheng, *RSC Advances*, 2013, **3**, 23638-23648.
54. J. C. Groen, L. A. A. Peffer and J. Pérez-Ramírez, *Microporous and Mesoporous Materials*, 2003, **60**, 1-17.
55. L. Wang, Y. Yu, P. C. Chen, D. W. Zhang and C. H. Chen, *Journal of Power Sources*, 2008, **183**, 717-723.
56. Z. S. Wu, S. Yang, Y. Sun, K. Parvez, X. Feng and K. Mullen, *Journal of the American Chemical Society*, 2012, **134**, 9082-9085.
57. K. H. Park, D. Lee, J. Kim, J. Song, Y. M. Lee, H. T. Kim and J. K. Park, *Nano letters*, 2014, **14**, 4306-4313.
58. S. J. Prabakar, Y. H. Hwang, E. G. Bae, S. Shim, D. Kim, M. S. Lah, K. S. Sohn and M. Pyo, *Advanced materials*, 2013, **25**, 3307-3312.
59. R. Wang, C. Xu, J. Sun, L. Gao and H. Yao, *ACS applied materials & interfaces*, 2014, **6**, 3427-3436.
60. R. Wang, C. Xu, M. Du, J. Sun, L. Gao, P. Zhang, H. Yao and C. Lin, *Small*, 2014, **10**, 2260-2269.

## Table of contents

Facile preparation of 3D Fe<sub>3</sub>O<sub>4</sub>/ macroporous graphene composite by self-assembly is proposed, and its superior Li storage performance against 2D Fe<sub>3</sub>O<sub>4</sub>/ graphene is revealed and deeply discussed.

